Optics and Lasers in Engineering 162 (2023) 107377

Contents lists available at ScienceDirect

Optics and Lasers in Engineering

journal homepage: www.elsevier.com/locate/optlaseng

Evaluating parametric uncertainty using non-linear regression in fringe projection

George Gayton*, Mohammed Isa, Richard K. Leach

Manufacturing Metrology Team, University of Nottingham, Nottingham, United Kingdom

A B S T R A C T

Optical coordinate measurement systems, such as fringe projection systems, offer fast, high-density measurements of arbitrary surface topographies. The versatility, speed and information density of fringe projection measurements make them attractive as in-situ measurement devices and autonomous inspection systems. However, the complex nature of the measurement process makes evaluating uncertainty from a fringe projection measurement complex – even in the hypothetical simple case where the accuracy of a measurement is limited only by the accuracy in the quantities that define a measurement from an indication; named system parameters here. In this paper, by validating a series of assumptions, a method to explore the uncertainty in the system parameters of a fringe projection system is given. The results of this investigation imply the common distortion model (the Brown-Conrady model) is not specific enough to the camera or projector of a fringe projection system to evaluate its uncertainty.

1. Introduction

Fringe projection systems are a type of optical coordinate measurement system (CMS) – similar in operation to laser line scanners and photogrammetry [1,2]. Fringe projection systems measure the surface of an object by recording the light reflected from an object's surface, and subsequently use the principles of triangulation to determine the surface as a collection of three-dimensional (3D) points, known as a point-cloud [3]. A fringe projection system consists of a two-dimensional (2D) fringe generator (e.g. a digital projector) and a number of cameras.

Fringe projection systems offer higher measurement speeds and denser point-clouds than traditional tactile CMS, without the need to physically touch a part. For these reasons, fringe projection systems are well-suited for in-situ measurements on the production line, avoiding the need to relocate parts elsewhere for inspection [4]. A fringe projection system can measure manufactured parts autonomously in real-time [5,6] or be used to augment an operators vision with augmented reality [7]. Also, a common problem in additive manufacturing machines is that existence of defects early in the build cost time and resources in continuing a faulty build – detecting defects in the build early using in-situ measurements may alleviate this issue [8]. Fringe projection systems are one of the few measurement systems capable of providing in-situ topography measurements of the additive manufacturing process [9–11].

Fringe projection lacks a standardised calibration method, which restricts the use of the technique in industry [12]. Measurement uncertainty is the quantification of the statistical dispersion of measurement values that can reasonably be attributed to the "true" value being measured. The standardised method of evaluating uncertainty is detailed in the Guide to the Expression of Uncertainty in Measurement (GUM) [13]. Without uncertainty, the disparity in measurements cannot be accounted for, and it will remain unknown as to how to treat any disparity in measurements. Therefore, measurement uncertainty allows the meaningful comparison of two measurements of the same object. Currently, fringe projection requires gauge repeatability and reproducibility (GR&R) tests on each individual measurement object [14]. Modern statistical techniques can evaluate uncertainty and do not require a unique evaluation for each measurement object [15] – but such methods still require an "extra" calibration step. In this paper, an extension to the calibration method [16] based on common regression techniques [17–19] will be explored for its applicability to fringe projection. The benefit of this method is no additional data is required – reducing the workload required in each fringe projection measurement.

A fringe projection system goes through what is often referred to as a "calibration", whereby a set of values are found that model the measurement value from the indication. In this paper, these set of values, henceforth referred to as "system parameters", model the 3D coordinates of the point-cloud from a set of images. Typically, each optical system, i.e. the cameras in a fringe projection system are modelled using the pinhole model with non-linear distortion parameters included [20]. The difference between metrological calibration defined above and calibration defined in relation to fringe projection is, unlike fringe projection calibration, metrological calibration provides an uncertainty in each of the system parameters. To distinguish this difference, calibration used in relation to fringe projection will be hereby referred to as "characterisation".

A common characterisation algorithm used in fringe projection estimates the system parameters using a non-linear regression [16,21]. It is

* Corresponding author.
E-mail address: ezxgg3@nottingham.ac.uk (G. Gayton).

https://doi.org/10.1016/j.optlaseng.2022.107377
Received 7 August 2022; Received in revised form 11 October 2022; Accepted 6 November 2022

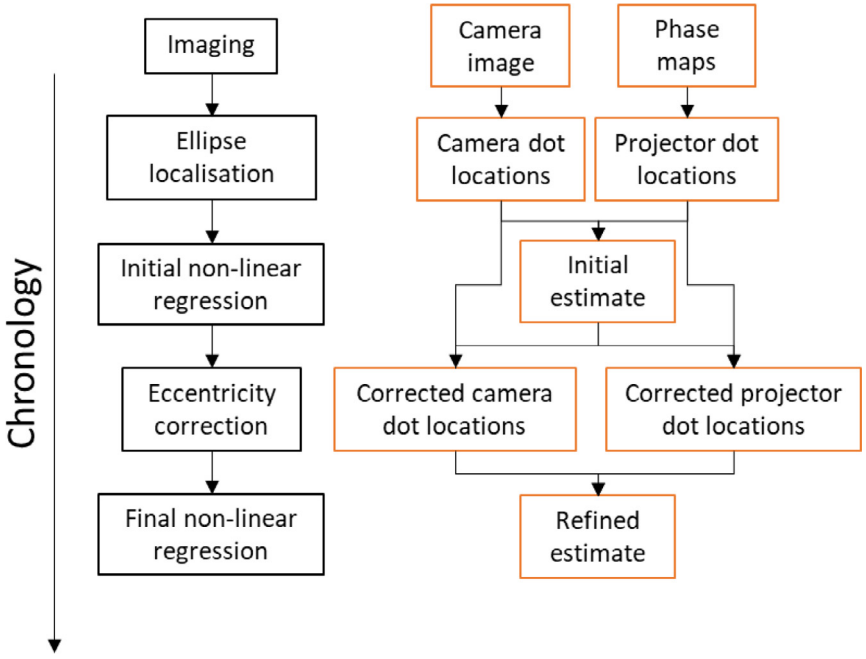

Fig. 1. The outline of the algorithm to localise the centres of dots within the camera and projector images.

possible, therefore, to obtain an estimate of the covariance matrix of the system parameters or propagate an uncertainty from regression inputs through to the parameters [18], but this is not commonly done. This paper attempts to reconcile the difference between a fringe projection characterisation and metrological calibration by exploring the validity of using the non-linear regression approach to evaluate an uncertainty in the system parameters.

In addition to the system parameters, there are many other factors that will influence the outcome of a measurement from a fringe projection system. The contribution that the measurement object's surface characteristics [22] and camera pixel noise [23] have on errors in the measurement is documented elsewhere [24–26]. In this work, only the contribution to the uncertainty of system parameters to the measurement uncertainty is considered.

This paper is structured as follows: first, a characterisation method based on non-linear regression is given, where a novel dot localisation algorithm based on weighted total least-squares is used to evaluate the uncertainty in the features localised within image planes. Then, the feature locations and their uncertainty are used for the first time to construct a weighting matrix to be used in a non-linear regression to estimate the system parameters, as well as to evaluate their uncertainty. For estimations made by the non-linear regression to be valid, certain conditions must be met – in the next section, three validation tests are given that test these conditions, namely specificity, linearity and a novel test for parameter equilibrium is given. Finally, the parameters and their uncertainty are tested on a flatness artefact and compared with a characterisation made using OpenCV 4.5.5 [27] and measurements made using a commercial fringe projection system.

1.1. Characterisation

In this section, the characterisation method is outlined, starting with the feature localisation within both the camera and projector images, and ending with the non-linear regression of the system parameters using the feature locations. Typically, planar checkerboards are used for feature localisation in camera characterisations [16,28], although alternative artefacts include random dots targets [29], noise-like targets [30] and active targets [31–33]. Another common pattern is the dot grid [34], which is generally favoured for fringe projection characterisation [21], but must have the eccentricity in the feature localisation corrected [35,36]. The dot grid has been chosen in this paper for its simplicity and ability to easily localise projector points.

Each dot in the dot grid will be imaged by the camera as an approximately elliptical shape. For convenience, this shape will be named as an ellipse throughout the rest of this paper. The feature localisation, therefore, returns the centres of each ellipse, with an uncertainty evaluated for both the camera image and inferred projector image. The artefact features (dot centres) do not project to the localised ellipse centres and so must be corrected – the eccentricity correction method used here is given elsewhere [37]. The eccentricity correction is assumed to be small, therefore, an initial non-linear regression is used to estimate the eccentricity correction, before the regression is repeated with the corrected feature locations. Alternative dot localisation techniques can be found elsewhere [35,36].

The characterisation can be summarised by five processes, given in Fig. 1. After acquisition of images, features are localised within the camera and projector image planes. The initial localisation estimate is used to both correct the feature locations during the eccentricity correction step to propagate uncertainty in the dot features to the camera and projector features.

The imaging step begins with a start-up procedure, to allow thermal equilibrium to be reached in the camera and projector prior to taking any measurements, followed by the acquisition and decoding of the camera images. A single image is used to localise the ellipse locations in the camera image plane. Then, a series of images of projected sinusoids are decoded to give a one-to-one correspondence of camera pixel to projector pixel, called the phase map – the method used in this paper in given elsewhere [38]. Since the dot grid is on a plane, the phase map can be expected to be absent of high-spatial frequency components [39] – remaining high-spatial frequency components are considered noise and can be filtered out. The cut-off frequency is chosen to remove high-spatial frequency noise without excessively corrupting the surrounding phase map with the ellipse boundary. The filter is chosen to be a Gaussian filter with width $\sigma = 0.28$ pixel^{-1}.

2. Image ellipse localisation

The camera ellipses are localised entirely using a single image acquired during the imaging step. Gradient methods are robust methods

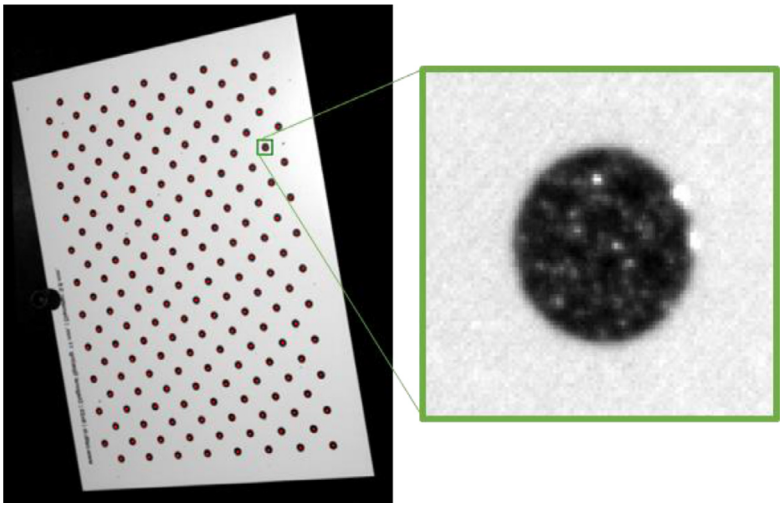

Fig. 2. Rough estimation and extraction of an imaged ellipse from a dot grid artefact and its surrounding area.

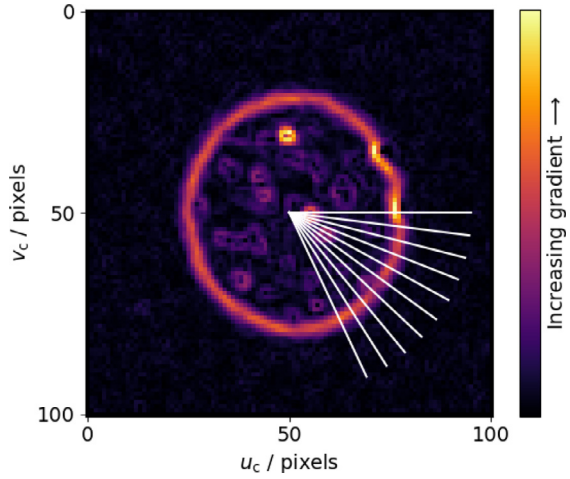

Fig. 3. Gradient image with radially expanding line-spread functions from the estimated ellipse centre.

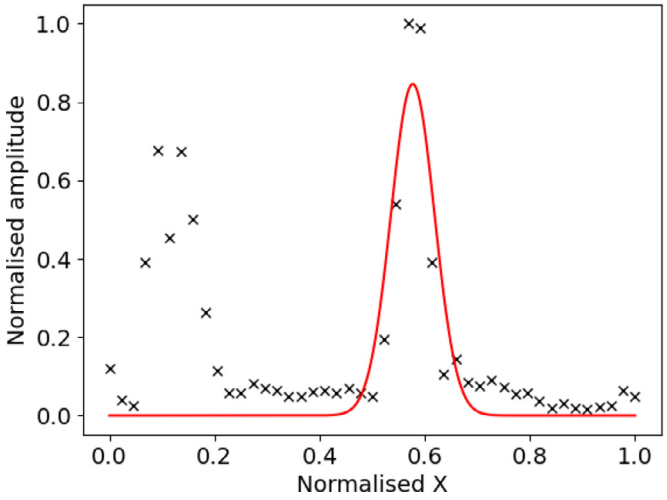

Fig. 4. Gaussian function (red) fitted to the line-spread function (black).

for fitting ellipses within camera images [40] and, therefore, will form the basis of the method used in this paper. The camera ellipse locations are found by estimating ellipse boundary points from the sub-pixel gradient peak of a line-spread function taken radially from an estimated ellipse centre. It is assumed that ellipse boundaries are located at the gradient peaks. First, a rough ellipse centre location is found using circular blob detection [41] in OpenCV. A typical measurement is given in Fig. 2, where a poorly imaged ellipse has been highlighted. There are several obvious issues with this dot; there are some specular reflections corrupting the edge and inside of the dot – the feature localisation algorithm must be robust against specular reflections.

A small region of the image centred on the estimated dot location rounded to the nearest integer is extracted. The gradient image of the small region is found using a convolution with a Sobel filter. A series of line-spread functions of the gradient image are taken radially from the estimated centre of the ellipse. It is assumed that the initial ellipse estimation is within ± 1 pixel. The number of line-spread functions are chosen so that each will be independent of each other at the ellipse boundary. The line-spread function is interpolated from the gradient image using a bilinear interpolation. The gradient image along with the cross-sectional lines is given in Fig. 3.

Each line-spread function is used to find the sub-pixel location of the boundary of each ellipse. Each line-spread function is fitted with a Gaussian function, given by

$$y = g(x, A, \mu, \sigma) = Ae^{-\frac{(x-\mu)^2}{2\sigma^2}} \tag{1}$$

where the parameters A, μ, σ are the peak height, peak centre and peak width respectively, to be found during the fitting. All line-spread functions are refined together during a single non-linear regression using the Levenberg-Marquardt algorithm. The peak width σ is a dot-specific parameter that is shared by all line-spread functions. The peak height A and the peak centre μ are line-specific parameters. A Gaussian function fitted to a line-spread function interpolated from a cross-sectional line shown in Fig. 3 is given in Fig. 4. The gradients of Eq. (1) all contain a $e^{-\frac{(x-\mu)^2}{2\sigma^2}}$ term, that will quickly go to 0 away from the peak centre μ. Significant noise such as the peak located at $X \approx 0.1$ in Fig. 4 will, therefore, have no effect on fitting to the appropriate peak located at $X \approx 0.6$, effectively filtering the noise away from the peak centre given the initial estimate of sufficient quality.

Across all line-spread functions, it is possible for Gaussian peaks to be fitted at incorrect positions or that the peak itself is significantly corrupted by noise. The outliers in the peak centre estimations are detected using a random sample consensus (RANSAC) algorithm, where point error and the least-squares ellipse fits are given elsewhere respectively [42,43]. Points are labelled erroneous if the magnitude of the point-to-ellipse boundary distance is larger than three standard deviations,

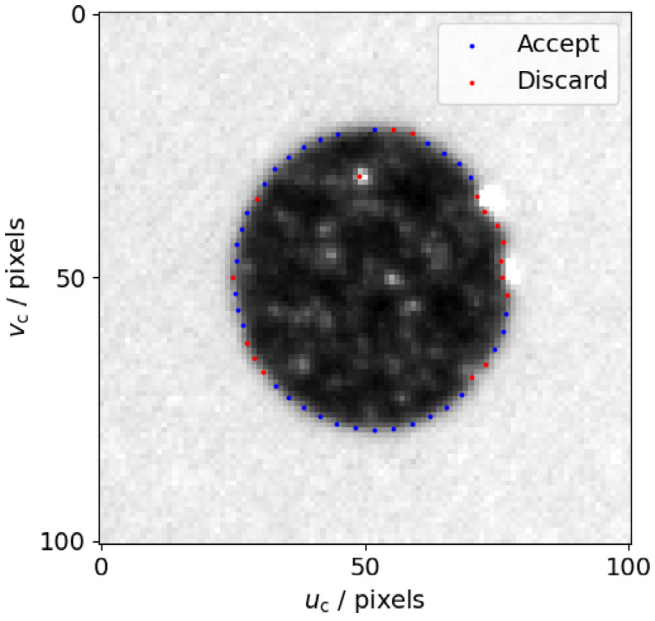

Fig. 5. The located sub-pixel boundary of an imaged ellipse.Points that have been found to be erroneous are coloured red; remaining points are coloured blue.

taken over the entire ellipse. The estimated boundary points of the ellipse given in Fig. 2 are shown in Fig. 5, with erroneous points filtered using the RANSAC algorithm.

Unlike weighted total-least squares, ordinary least-squares estimation will neglect error in the regressors, which is problematic in the least-squares ellipse fits [43], since the regressor values are erroneous and correlated. The weighted total least-squares method given here is taken from Ref. [44] and adapted to the least-squares method in Ref. [43]. An alternative unweighted total least-squares method to estimate ellipses is given elsewhere [45]. The novelty here is that this is the first time a weighted total least-squares method is applied to ellipses for the application of characterisation of a fringe projection system (to our knowledge). The standard uncertainty in boundary points is shown in Fig. 6(a), and the standard uncertainty of the ellipse is shown Fig. 6(b).

The projector ellipse centres are found by applying a linear transform to the estimated ellipse centre in the camera image. The dot grid is located on a plane, so the mapping is given by a rational function [46]. However, locally the mapping can be considered linear. Errors can be propagated from the elliptical centres, along with the transform, using the propagation of uncertainty given in the GUM [13]. A small region surrounding the ellipse centre is extracted from the phase map. The ellipse centre and its boundary pixels will not give accurate mapping data because of the low contrast of any reflected fringes and must be discarded. These areas are discarded by removing pixels within an ellipse with axes expanded by eight pixels. The local camera to projector coordinate transform is found using least-squares regression. It is also noted that the errors in projector coordinates will give rise to autocorrelation, but since the number of observations are high, the errors are assumed to asymptotically follow a normal distribution. The residual of the linear mapping function in the cropped region after fitting is given in Fig. 7.

2.1. Non-linear regression

The use of non-linear regression in camera characterisation was introduced in Ref. [16], and extended to fringe projection systems in Refs. [21] and [47]. In general, non-linear regression estimates the parameters $\vec{\theta}$ that satisfy the function

$$\vec{y} = f\left(\vec{x}, \vec{\theta}\right), \tag{2}$$

where $\vec{y}$ is some measured output and $\vec{x}$ is a known input. The estimation is completed by minimising the function

$$\|\hat{y} - f\left(\vec{x}, \vec{\theta}\right)\|, \tag{3}$$

where $\hat{y}$ represents an imperfect realisation of the true $\vec{y}$. The Levenberg-Marquardt algorithm is an algorithm to minimise Eq. (3), by iteratively improving an estimate of the parameters $\vec{\theta}$ using local gradient matrices, known as the Jacobian $\mathcal{J} = \nabla_\theta f(\vec{x}, \vec{\theta})$. From an epicentre $\vec{\theta}_e$, a vector $\vec{\delta} = \vec{\theta} - \vec{\theta}_e$ can be found that minimises Eq. (2), given by

$$\left(\mathcal{J}^T\mathcal{J} + \lambda \mathrm{diag}\left(\mathcal{J}^T\mathcal{J}\right)\right)\vec{\delta} = \mathcal{J}^T\vec{\epsilon} \tag{4}$$

where $\vec{\epsilon} = \vec{y} - f(\vec{x}, \vec{\theta}_e)$, λ is a damping factor and the diag operator returns its argument with non-zero values only in the diagonal. Eq. (4) is solved successively until some condition is true, such as the failure to reduce Eq. (3), and is guaranteed to at least find the local minimum [17]. In fringe projection, $\vec{x}$ is a set of features of known relative position, $\vec{y}$ is the locations of the features within the camera and projectors images, and the function f describes the projection of feature position $\vec{x}$ to image location $\vec{y}$. The Levenberg-Marquardt algorithm requires an approximate solution, which can be found analytically, given some assumptions [16]. Heteroscedasticity is problematic in non-linear regression, and typically a requirement for a successful regression is that the errors in the vector $\vec{\epsilon}$ be uncorrelated. The heteroscedasticity issue is alleviated using a weighting matrix in the optimisation, altering Eq. (4) to give

$$\left(\mathcal{J}^T\boldsymbol{W}\mathcal{J} + \lambda \mathrm{diag}\left(\mathcal{J}^T\boldsymbol{W}\mathcal{J}\right)\right)\vec{\delta} = \mathcal{J}^T\boldsymbol{W}\vec{\epsilon}, \tag{5}$$

with $\boldsymbol{W} = \boldsymbol{V}_\epsilon^{-1}$. The covariance matrix $\boldsymbol{V}_\epsilon$ describes the covariance of vector $\vec{\epsilon}$, which is a function of known features $\vec{x}$, measured feature image location $\vec{y}$ and parameter estimation $\vec{\theta}_e$.

If the linearization approximation used here holds, the region for which the parameter solution exists can be considered linear. For a linear system given by $\vec{y} = \boldsymbol{X}\vec{\theta}$, where the covariance matrix of the observations $\vec{y}$, given as $\boldsymbol{V}_y$ is known, the covariance matrix of the parameters $\vec{\theta}$, given by $\boldsymbol{V}_\theta$, is defined then the parameter covariance matrix $\boldsymbol{V}_\theta$ is given by

$$\boldsymbol{V}_\theta = \left(\mathcal{J}^T\boldsymbol{V}_\epsilon^{-1}\mathcal{J}\right)^{-1}, \tag{6}$$

where $\boldsymbol{V}_\epsilon$ is the covariance matrix of the vector $\vec{\epsilon}$. The estimate $\vec{\theta}$ defined during the non-linear regression is only valid under specific conditions – given in Section 3. The calculation of the weighting matrix is a function of the observation $\vec{y}$ (the ellipse centres), the regressor $\vec{x}$ (the artefact dot positions) and the estimated parameters $\vec{\theta}$, and can be found by propagating uncertainty using

$$\boldsymbol{V}_\epsilon = \boldsymbol{V}_y + \mathcal{J}\boldsymbol{V}_x\left(\vec{x}, \vec{\theta}\right)\mathcal{J}^T, \tag{7}$$

where the covariance matrix $\boldsymbol{V}_x$ has its dependence explicitly stated here for clarity. Covariance matrix $\boldsymbol{V}_\epsilon$ can be updated each iteration using the updated parameter estimate $\vec{\delta} + \vec{\theta}$ following Eq. (5) or alternatively, under the assumption that $\boldsymbol{V}_\epsilon$ is approximately constant near the solution locus, can be calculated just once using the initial approximation of $\vec{\theta}$, which is used in this paper.

2.2. Regression regimes

The system parameters $\vec{\theta}$ can be estimated in one pass, regressing parameters in both the camera and the projector simultaneously, or they can be estimated separately. This paper will explore four methods to characterise fringe projection systems: the parallel method that estimates all parameters in a single regression; the weighted parallel method that modifies the parallel method with a weighting matrix; the serial method that estimates the camera parameters followed by the projector parameters and the extrinsic estimates; and the weighted serial method that modifies the serial method with a weighting matrix. Estimating parameters in parallel reduces the total degrees of freedom of

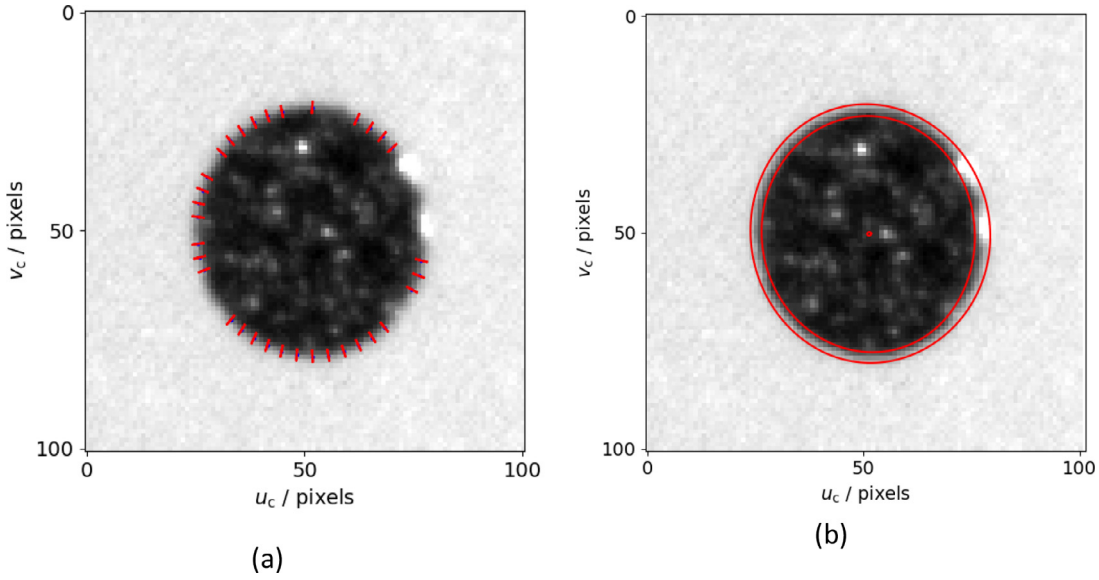

Fig. 6. Uncertainty of the imaged ellipses (a) boundary and (b) ellipse centre and perimeter.

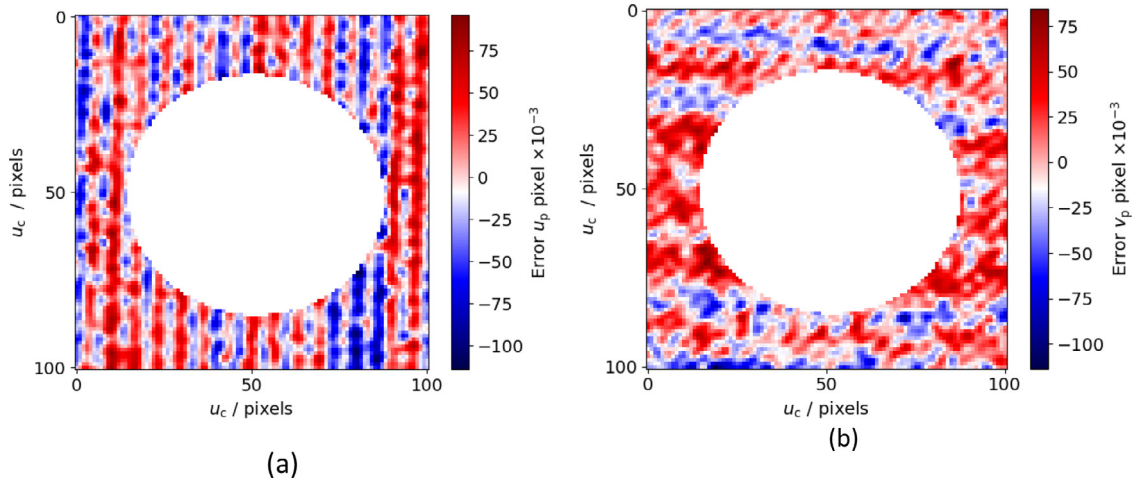

Fig. 7. Error in the camera-to-projector mapping of the (a) u-axis and (b) v-axis. The central white space is cropped out.

the regression since the artefact position and orientation must be estimated only once per view. However, this will increase both the level of correlation and the heteroscedasticity within the input data. In the case of fringe projection:

1. The projector and camera images have different scales, and since the reprojection error used to regress the parameters is calculated on the image plane, the projector and camera image points will have completely different uncertainty.
2. The projector ellipse image locations are inferred from camera ellipse image locations and are, therefore, correlated in some way and will have larger errors when compared at the same scale.
3. The same artefact provides repeated measurements, all repeated measurements of the same dot on the dot grid will be correlated in some way.

Additionally, the weighting matrix $\boldsymbol{W}$ can become significantly large. It is typical to use more than twenty-five positions within the characterisation to ensure there is enough data redundancy and image plane coverage. Given there are N_{pos} number of positions, N_{art} number of points on the artefact, and each point has two degrees of freedom and is measured once in the camera and once in the projector, the regression has $N_{\text{pos}} \times N_{\text{art}} \times 2 \times 2$ degrees of freedom. Given an artefact containing 184 points measured in twenty-five positions, the weighting matrix has the size 18,400×18,400, with significant off-diagonal terms. In this paper, to reduce memory requirements, artefact points are only used once in either the camera or projector image plane, reducing the computational complexity roughly by a factor of sixteen. In systems with multiple cameras and projectors, it may be impossible to conduct the parallel regression.

3. Characterisation results

This section will detail the outcome of the characterisation. A total of twenty-seven unique positions and orientations of the board were imaged to create 2592 camera points and 2376 projector points. Each position is shown in Fig. 8 and the parameter estimations are given in Table 1. The camera/projector matrix parameters follow those given in Ref. [16], the distortion parameters follow the Brown-Conrady distortion model [48–50] and the rotation parameters q_1, q_2, q_3 follow the Rodrigues rotation convention.

Some parameters—the focal lengths, principle points and extrinsic values of both the camera and projector—are similar regardless of the method or weighting matrix used. There are significant differences when looking at distortion parameters and the skew parameter – there may be

Table 1
Parameter estimations.

	Unit	Description	Parameter	Serial	Weighted serial	Parallel	Weighted parallel
Camera matrix	pixel	Focal lengths	f_x	8520	8536	8510	8534
			f_y	8485	8536	8477	8535
		Skew	s	20.00	−0.4431	20.11	−0.4917
		Optical centres	u_0	2674	2676	2674	2675
			v_0	2544	2538	2543	2537
Camera distortion	–	Radial parameters	k_1	−0.0158	−0.0339	−0.0173	−0.034
			k_2	−0.0323	0.1264	−0.0263	0.1219
			k_3	0.0541	−0.1619	0.0452	−0.1891
		Tangential parameters	p_1	−0.0070	−0.0011	−0.0069	−0.0011
			p_2	0.0019	−0.0004	0.0020	0.0004
		Distortion centres	u_{dc}	−0.0771	−0.0097	−0.0779	−0.0094
			v_{dc}	0.2730	0.0070	0.2679	0.0060
Projector matrix	pixel	Focal lengths	f_x	1123	1121	1121	1121
			f_y	−2247	−2243	−2242	−2242
		Skew	s	−0.2423	0.0083	−0.3997	−0.2741
		Optical centres	u_0	443	442	443	443
			v_0	1187	1187	1186	1187
Projector distortion	–	Radial parameters	k_1	0.0495	0.0543	0.0579	0.0551
			k_2	−0.1765	−0.1906	−0.2236	−0.1942
			k_3	0.0845	0.0960	0.1461	0.1000
		Tangential parameters	p_1	0.0006	0.0001	0.0007	0.0001
			p_2	0.0002	0.0002	0.0002	0.0002
		Distortion centres	u_{dc}	−0.0033	−0.0042	−0.0062	−0.0048
			v_{dc}	0.0121	0.0167	0.0252	0.0175
Projector extrinsics	–	Rodrigues rotation vector components	q_1	0.2659	0.2651	0.2654	0.2651
			q_2	−0.2823	−0.2830	−0.2830	−0.2830
			q_3	1.5706	1.5719	1.5707	1.5719
	mm	Translation vector components	t_x	5.7123	5.6859	5.7361	5.6857
			t_y	306.3578	306.3366	306.4418	306.2259
			t_z	−44.3868	−44.4270	−44.2130	−44.4299

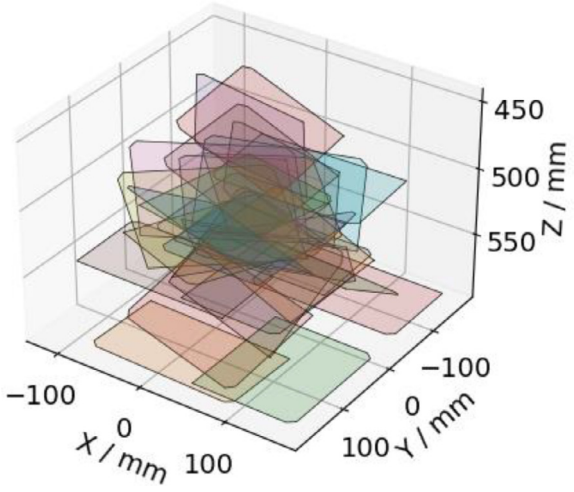

Fig. 8. Location of the twenty-seven board locations and orientations used for the characterisation.

more than one solution to the regression. The choice of regression mode is critical for parameter estimation, while the use of weighting matrix reduces this difference. The parameter correlation matrices are shown in Fig. 9.

In Fig. 9, there is a high degree of similarity in parameter correlation estimation when using a weighting matrix, with some missing correlation between the camera, projector or extrinsic parameters, since the serial method regresses camera and projector parameters independently.

The point spread function (PSF) describes the response of an imaging system to a point source or point object and is related to a line-spread function [51]. The line-spread function found during the dot localisation could potentially be used to estimate a spatially-variant PSF. The peak width estimated from each line-spread function across the ellipse boundary is given, shown in Fig. 10.

Without further data collection, the ellipse localisation method is also able to estimate the camera's field of view. This method will be used in future uncertainty evaluations that consider the limited optical resolution of the camera. This is a secondary result from this method and will not be considered further in this paper.

3.1. Validation

For the parameter and covariance estimation of the non-linear regression to be valid, a series of conditions must be valid:

Specificity. Given there are no errors in the regressor vector $\vec{\boldsymbol{x}}$ or the observation vector $\vec{\boldsymbol{y}}$, the function $f(\vec{\boldsymbol{x}}, \vec{\boldsymbol{\theta}})$ must accurately predict $\vec{\boldsymbol{y}}$. A model that does not comply with this condition is known as misspecified, and the covariance matrix estimate $\boldsymbol{V}_\theta$ given in Eq. (6) will be invalid.

Linearity. The linearisation used to estimate the parameters in the non-linear regression must accurately represent the function over a small interval. A model that is significantly non-linear will not be well approximated by a first-order Taylor approximation, and while the parameter estimate $\vec{\boldsymbol{\theta}}$ may still be correct, the covariance estimate $\boldsymbol{V}_\theta$ given in Eq. (6) will be invalid.

Equilibrium. The characterisation occurs over a finite time-period where it is assumed that the parameters under investigation do not vary. However, optical parameters are dependant on temperature that can cause them to vary across the regression. A failure in the equilibrium condition will result in invalid parameter and covariance estimations.

Normality. The errors introduced in the measurements must follow a Gaussian distribution. If the errors do not follow a Gaussian distribution, then the input uncertainty $\boldsymbol{V}_\epsilon$ is incorrect and there will be unaccounted errors propagated to the solution $\vec{\boldsymbol{\theta}}$.

In this section, tests for specificity, linearity and equilibrium are presented. Given the number of observations used in the characterisation, it is assumed that the errors asymptotically follow a normal distribution.

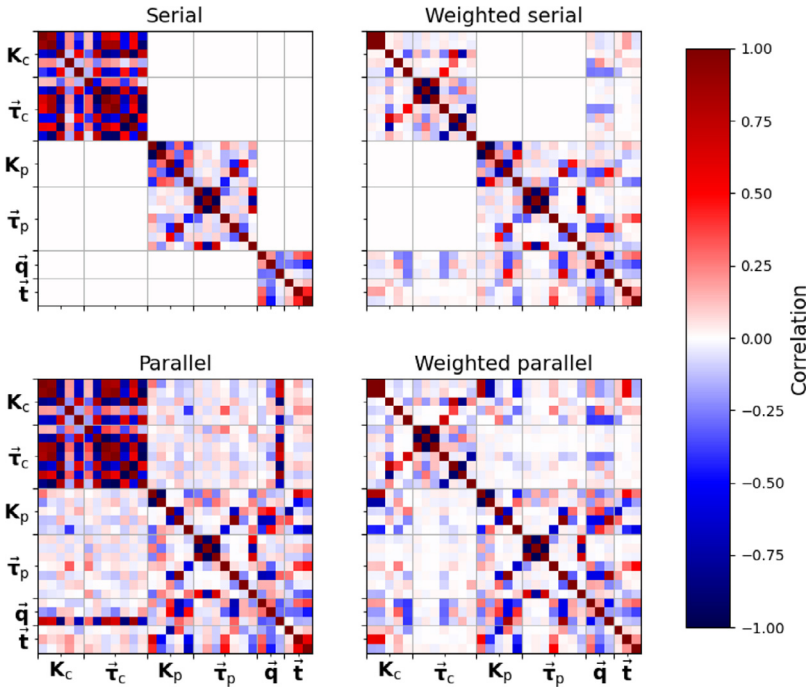

Fig. 9. Correlation matrix of the parameter estimate from each characterisation method.

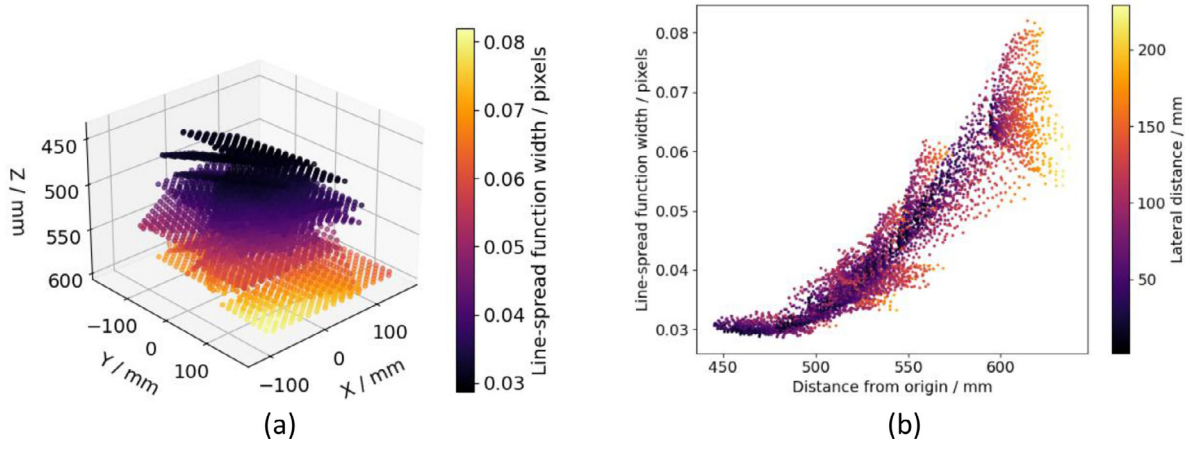

Fig. 10. The width of the Gaussian line-spread function in (a) 3D and (b) plotted against distance from the camera pinhole origin. The lateral distances in (b) correspond to the distances along the XY coordinates from the origin (0,0,0).

3.2. Specificity

White's specificity test [52] is used to test the specificity of the model for the non-linear regression in the characterisation. The specificity test verifies whether the model used in the linear regression is correct up to some additive error, otherwise the implication is there are variables excluded from the model. For a non-linear regression that, in the final step, computes the Jacobian $\mathcal{J}$ and the residuals $\vec{\epsilon}$ at the solution $\vec{\theta}$, the specificity test [52] is given by finding the solution $\vec{\alpha}$ to

$$\vec{\epsilon}^2 = a_0 \odot \vec{1} + \psi\vec{a}, \tag{8}$$

$$\boldsymbol{\psi} = \mathcal{J} \odot \mathcal{J}, \tag{9}$$

with $\odot$ being the Hadamard product. The test will fail if there is a solution to Eq. (8) that has some sufficient statistical power, i.e., if the square residual $\vec{\epsilon}^2$ can be modelled in some way. Given there are N_{pos} observations and P parameters being estimated in the non-linear regression, the test is completed by computing n times the constant-adjusted coefficient of determination, $n \times R^2$ and comparing to a critical value from the χ^2 distribution. It has been shown [52] that the specificity test will also fail in the presence of heteroscedasticity. In Section 2, the covariance (and by extension the correlation) between image points were estimated and are given in covariance matrix $\boldsymbol{V}$. The correlation can be removed using the transform $\boldsymbol{C}^{-1}$, where $\boldsymbol{C}\boldsymbol{C}^{\mathrm{T}} = \boldsymbol{V}$. The transforms $\vec{y}' \to \boldsymbol{C}^{-1}\vec{y}$ and $\mathcal{J} \to \boldsymbol{C}^{-1}\mathcal{J}$ gives the updated equations

$$\left(\boldsymbol{C}^{-1}\vec{\epsilon}\right)^2 = \alpha_0 + \boldsymbol{\psi}'\vec{\alpha}, \tag{10}$$

$$\boldsymbol{\psi}' = \left(\boldsymbol{C}^{-1}\mathcal{J}\right) \odot \left(\boldsymbol{C}^{-1}\mathcal{J}\right). \tag{11}$$

The specificity test will now additionally fail if the covariance matrix $\boldsymbol{V}$ is not correct up to a scalar multiplicative error, or if the model is not correct up to an additive error, given a scalar multiplication will cancel in Eq. (10). However, unlike the serial method, the parallel method is sensitive to a scalar multiplicative error, considering the covariance matrix is a concatenation of the projector and camera regressor covariance matrices.

The characterisation measures the artefact in twenty-seven positions, giving five pinhole parameters, seven distortion parameters and 27×6

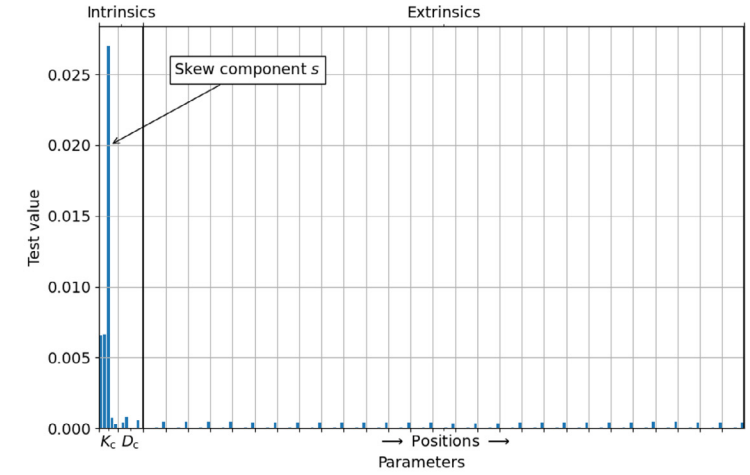

(a)

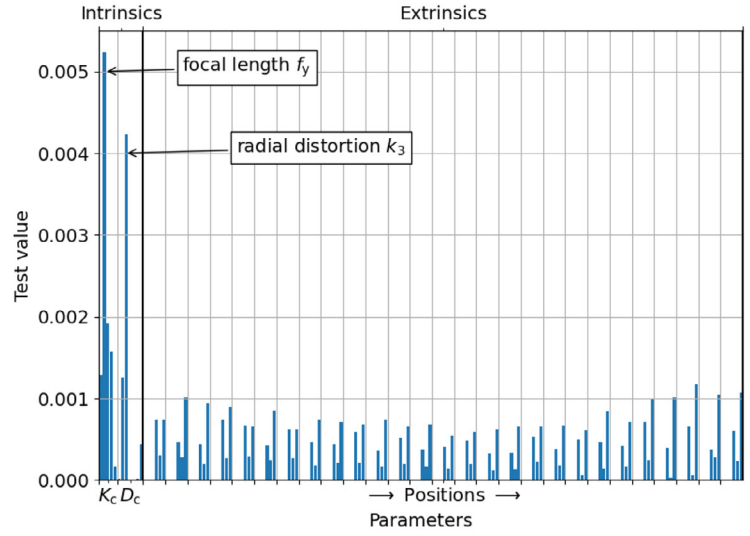

(b)

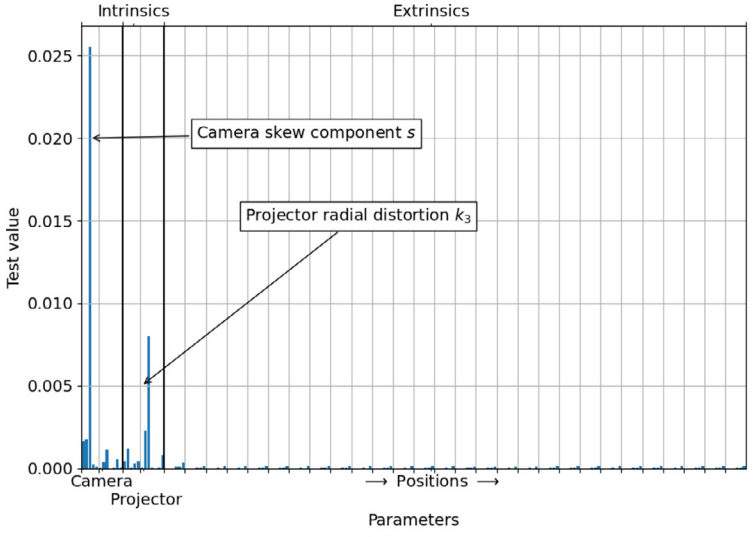

(c)

Fig. 11. The Clarke curvatures Γ of the system parameters. (a-b). Camera and projector parameters estimated using the serial method. (c) Parameters estimated using the parallel method.

Table 2
Specificity test results for the weighted serial and weighted parallel method.

	Test value	Critical value
Weighted serial (camera)	880	206
Weighted serial (projector)	1116	206
Weighted parallel (all)	5560	225

extrinsic parameters, for a total of 174 parameters. The critical value of the χ^2 distribution with 174 degrees of freedom is 206, i.e., 95% of values are expected to be below 206. In the parallel characterisation, there are ten pinhole parameters, fourteen distortion parameters and an additional six parameters describing the rotation and translation from the camera coordinate system to the projector coordinate system, giving a total of 192 parameters. The critical value of the χ^2 distribution with 174 degrees of freedom is 225. The results of the specificity test are given in Table 2.

This specificity test [52] simultaneously tests the covariance matrix of inputs used in the characterisation and the model. The specificity test fails for both methods and has a higher failure rate in the parallel method. The optical distortion in the projector is higher than in the camera – which implies that the distortion model is inadequate for measurement accuracies at the level made in the characterisation. The failure could also indicate that the covariance matrix estimation $\boldsymbol{V}_{\epsilon}$ is poor. The higher test score in the parallel method would imply that there is a scalar multiplicative error in the regressor covariances matrices – given that only the parallel test score is sensitive to this error.

3.3. Linearity

In this section, the non-linearity on the parameter covariance estimate in a non-linear regression will be tested. Given the characterisation uses a linear approximation of a non-linear problem, significant non-linearity will invalidate the linear approximations and reduce the efficacy of the covariance estimation. The measure of nonlinearity used in this paper is the Clarke curvature Γ_j [53]. If the condition $|\frac{1}{2}\Gamma_j sc| < 0.1$ is true, then the curvature is considered acceptable enough to obtain a reasonable covariance matrix. The results of the Clarke curvatures for the weighted serial and weighted parallel methods are given in Fig. 11.

The non-linearity is well within acceptable limits. The parameter with the highest non-linearity measure is the skew component in the pinhole matrix of the camera. Ref. [54] shows that an increase in the number of observations can reduce the non-linearity – in a characterisation with fewer observations, it may be prudent to remove the skew component of the pinhole camera matrix. The projector, however, does not show the same behaviour.

3.4. Equilibrium

The equilibrium test given in this section takes advantage of the spare degrees of freedom left in the serial characterisation method. The serial characterisation method gives N_{pos} estimations of the position of the dot grid for both the camera and projector and, therefore, each estimation of the artefact orientation and position can be tested for consistency – preventing an undetected failure of the equilibrium condition. The test will also fail if the linear regression conditions are broken or if the uncertainty matrices are $\boldsymbol{V}_{\epsilon}$ are poor, and if there is no indication of what condition has been invalidated during a failure.

The serial characterisation method gives a weighted estimation of the extrinsic parameters (the Rodrigues rotation vector $\vec{q}$ and translation $\vec{t}$) describing the transform between the camera and the projector, along with an uncertainty. For the unweighted serial method, this is found using an estimate of the parameter covariance matrix, given by the estimator

$$\boldsymbol{V}_{\theta} = \frac{\|\vec{\epsilon}\|}{N-P}\left(\mathcal{J}^{\mathrm{T}}\mathcal{J}\right)^{-1}, \tag{12}$$

where N equals the number of observations within the regression and P equals the number of parameters obtained from the regression. For the weighted serial method, the parameter covariance matrix is found using the weighted estimator,

$$\boldsymbol{V}_{\text{all}} = \left(\mathcal{J}^{\mathrm{T}}\boldsymbol{V}_{\epsilon}^{-1}\mathcal{J}\right)^{-1}. \tag{13}$$

With an estimated uncertainty of the parameters $\boldsymbol{V}_{\text{all}}$ obtained, each estimate of the camera-projector transform can be compared for agreement, i.e., whether there is any statistically significant deviation from the final estimate of the camera-projector transform. A χ^2 test can now be completed using

$$\left(\vec{\theta}_{\text{all}} - \vec{1}\otimes\vec{\theta}_{\text{e}}\right)^{\mathrm{T}}\left(\boldsymbol{V}_{\text{all}} + \boldsymbol{V}_{q,t}\otimes\mathbb{I}\right)^{-1}\left(\theta_{\text{all}} - \vec{1}\otimes\vec{\theta}_{\text{e}}\right), \tag{14}$$

where $\otimes$ is the Kronecker product. A comparison of the camera-projector transform estimates from each artefact with the final estimate is given in Fig. 12.

With some exceptions, the application of the covariance matrix has reduced the deviation of the quantity values. The critical value of a χ^2 distribution with $26 \times 6 = 162$ degrees of freedom is 192.7, where the unweighted serial method obtained a score of 1691.5, and the weighed serial method obtained a score of 80.4. The equilibrium test will also fail when the covariance matrix $\boldsymbol{V}_{\text{all}}$ is unable to explain the discrepancy in different camera-projector transforms for all artefact positions.

3.5. Measurement results

In this section, the system parameters, as well as the covariance matrix found during the characterisation, are tested using three measurements of a flatness artefact. A flatness artefact was chosen to minimise the effect that the surface geometry has on the measurement result [22]. The efficacy of the weighting matrix approach is compared through the assessment of the system parameters. The accuracy of the system parameters is evaluated using the spread of the deviation of points from a fitted plane – defined here as the flatness deviation.

A flat is chosen as the artefact to validate the calibration method in this paper over other artefacts, such as sphere dumbbells, for the following reasons. A flat provides the simplest measurement for fringe projection – there are no multiple reflections off the surface and the surface is absent of high spatial-frequencies allowing filtering of phase noise, see Section 4.1. Phase noise is the dominant source of error in a fringe projection system [48,55], the choice of artefact is key in providing a measurement that is limited by accuracy in the system parameters, instead of the phase noise.

The flatness deviation in measurements determined using the system parameters of all four characterisation methods, measurements determined using system parameters found using OpenCV's stereoCalibrate method and measurements made using a commercial system, the GOM ATOS Core 300, will be compared. Then, the uncertainty matrix of all four system parameters is evaluated using the same measurement of a flatness artefact, with a reduced χ^2 metric to test for the level of agreement with the reference deviation of the plane measured using a tactile CMS.

3.6. Flatness deviation analysis method

When determining the flatness deviation, any deviation from the best-fit plane caused by uncertainty in the system parameters will be additively combined with a phase error that dominates over the uncertainty from the system parameters. The correspondence decoding algorithm uses a periodic pattern to establish the link between camera and projector points. It is assumed, therefore, that the range of spatial

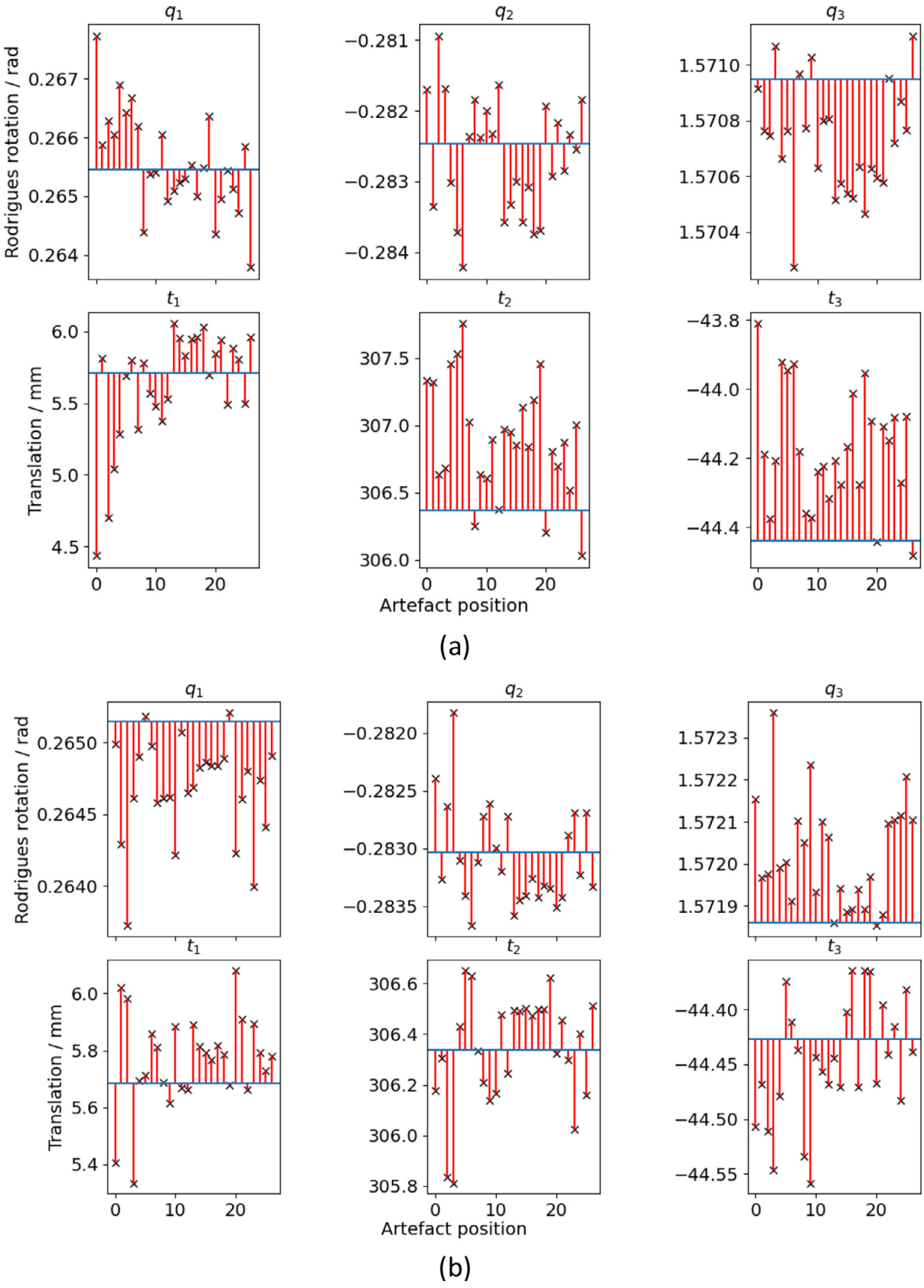

Fig. 12. Comparison of the twenty-seven estimations of the transform between the camera and projector.Estimation obtained using the (a) serial method and (b) unweighted serial method.

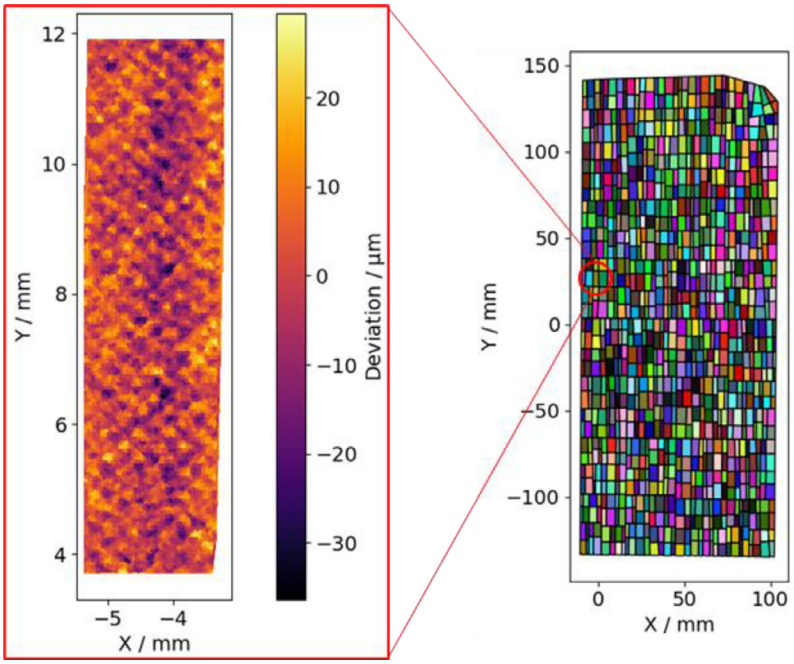

Fig. 13. Clustering algorithm used to derive the flatness deviation. (right) The flatness deviation values in a single cluster of points. (left) The clustered point-cloud, shown in the xy plane, where each colour represents a cluster that will make a pseudo-point.

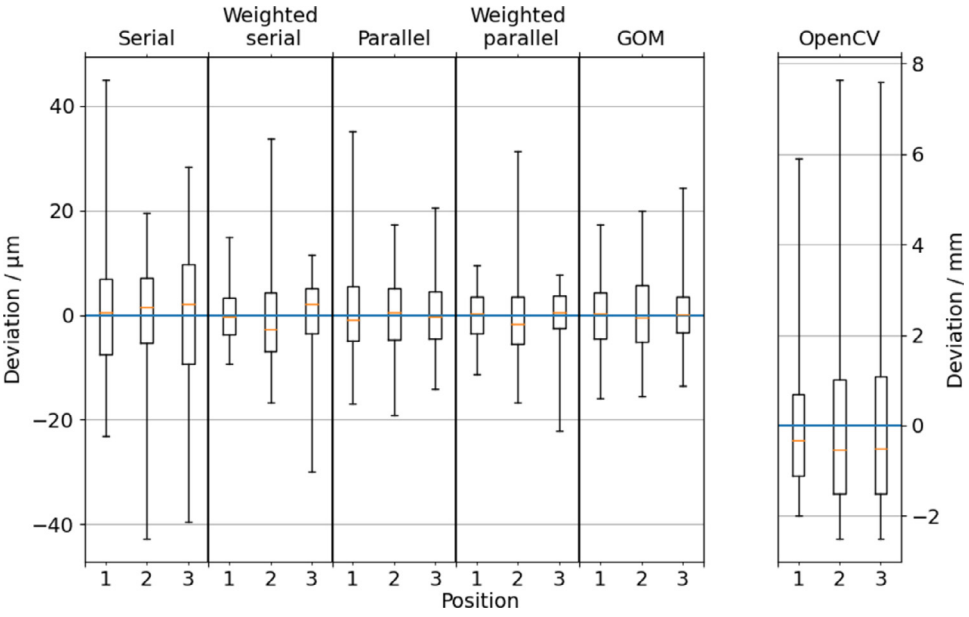

Fig. 14. Box plots of the range of flatness deviations across the entire flat, with the whiskers covering the full range of the data, and the box showing the inter-quartile range.

frequencies in the point-cloud caused by phase error will be limited to approximately the fringe period on the measurement surface. i.e., the form error caused by the system parameters will have much larger spatial frequencies in the measured points compared to the phase error. By averaging over a large enough area, any phase error should be significantly reduced.

Additionally, the flatness artefact is measured within a particular bandwidth of spatial frequencies on a tactile CMS. Fringe projection measurements have higher point density and typically measure a wider range of spatial frequencies. The analysis must remove higher spatial frequencies in the measurement data to compare with a known measurement of the flatness artefact containing only lower spatial frequencies. The point-cloud of the flatness artefact contains roughly 2×10^6 points and is reduced to 1024 pseudo-points using a clustering method based on Ref. [56] – the result can be seen in Fig. 13.

3.7. Comparison of flatness deviations

The accuracy of each set of system parameters is evaluated by comparing the flatness deviations in three measurements made using each set of system parameters, system parameters obtained using OpenCV and three measurements made using the GOM ATOS Core 300. The three positions of the flatness artefact were chosen so that every part of the image plane of the camera and projector were represented in at least one measurement. The spread of values in flatness deviation is shown in Fig. 14.

The weighting matrix significantly improves the accuracy of the serial characterisation method for every position and improves the parallel characterisation method in two of three positions. Both weighted methods give similar results – the weighting matrix is a useful tool to more appropriately define the loss function used in the characterisa-

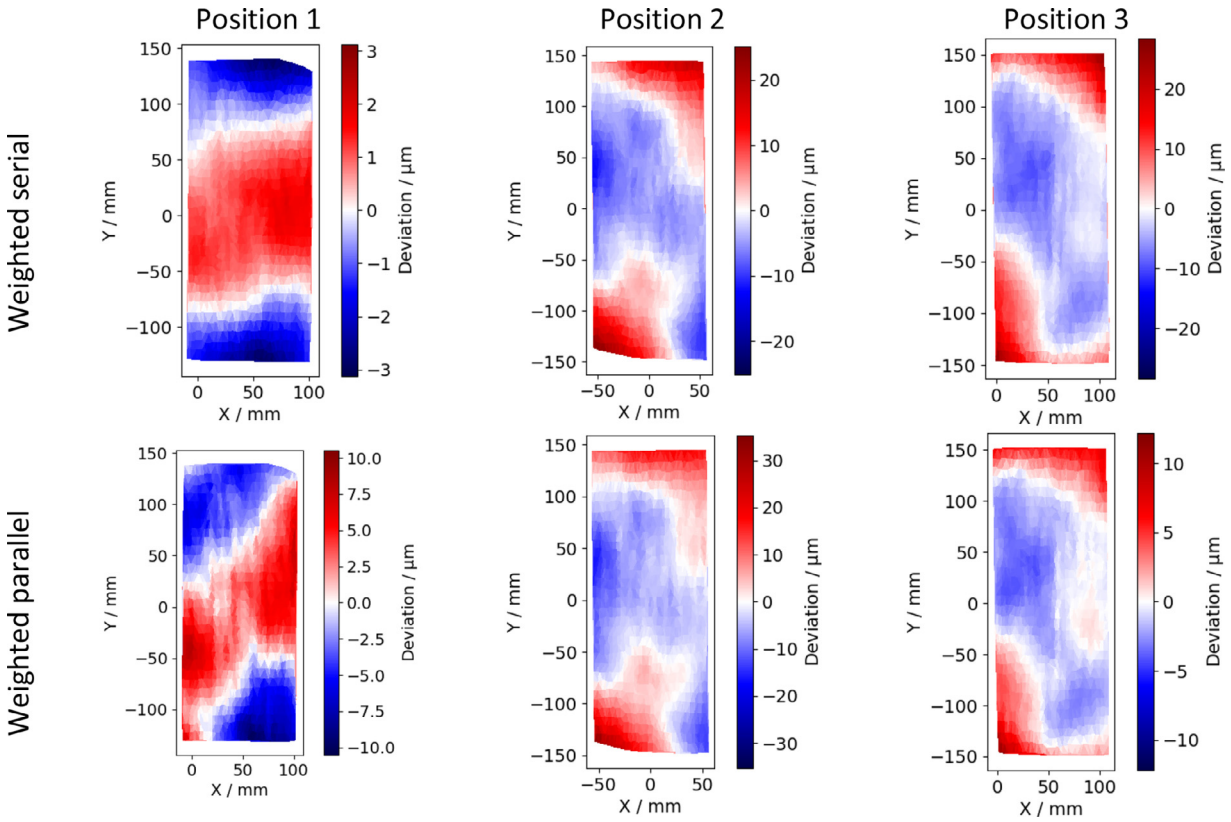

Fig. 15. Mean deviation of each data point from the substitute best-fit plane across the flatness artefact from the Monte-Carlo trials.

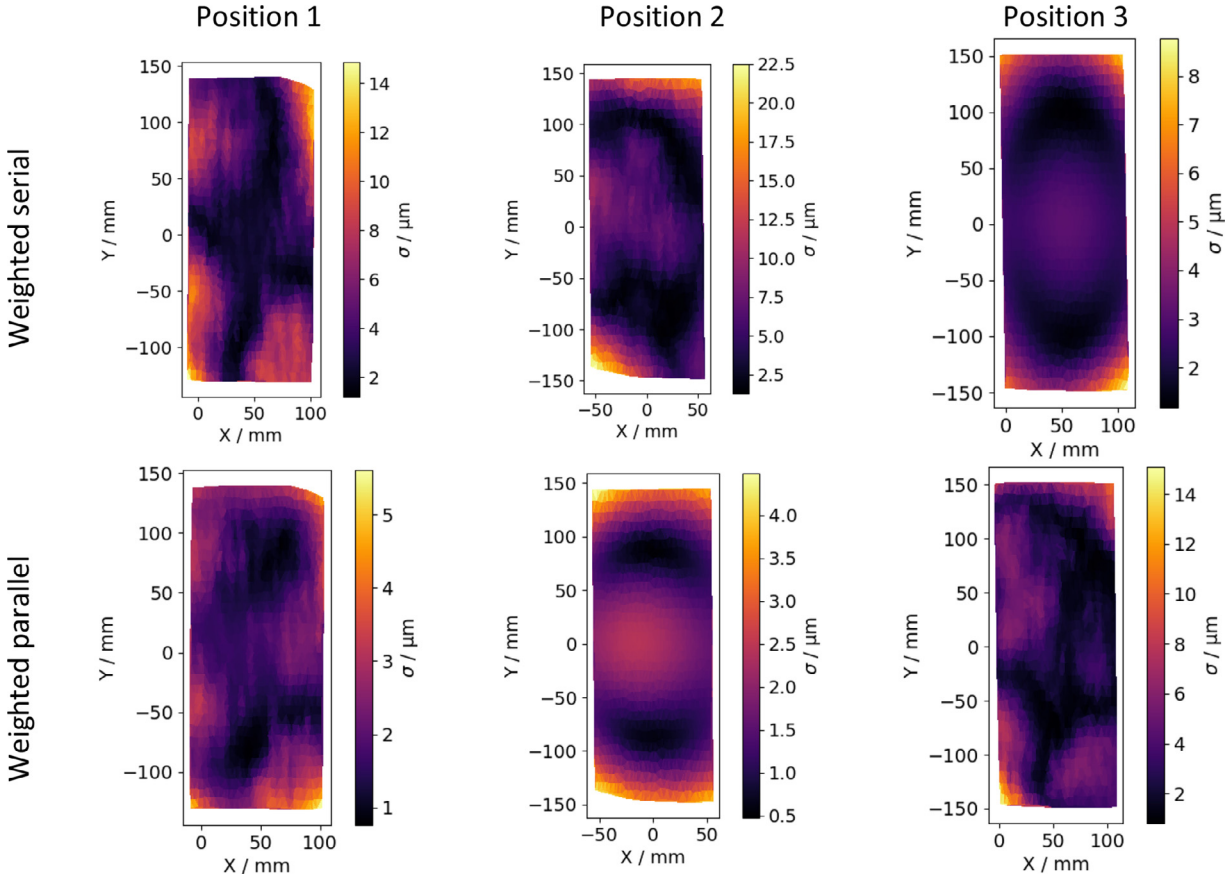

Fig. 16. Standard deviation of the deviation of each cluster point from the substitute best-fit plane across the flatness artefact from the Monte-Carlo trials.

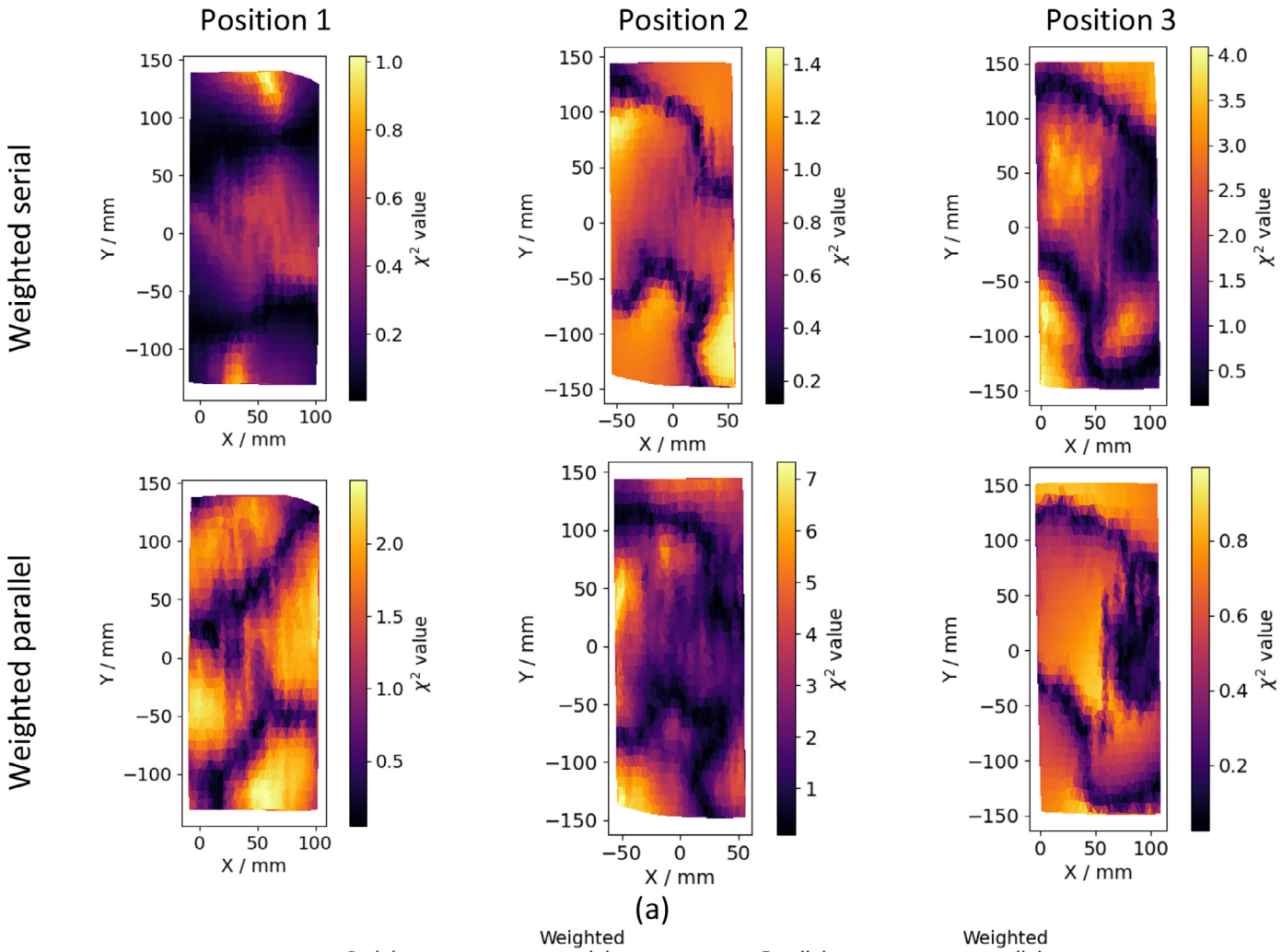

Fig. 17. χ^2 test results of each data point from the Monte-Carlo trials. Data is given in (a) 3D space and (b) collectively per measurement.

tion. The accuracy of both weighted methods is comparable to the GOM measurements, and far exceeds the OpenCV measurements, but are less reproducible than the GOM measurements. Note that unlike the comparison between the serial, weighted serial, parallel, weighted parallel and OpenCV methods, the GOM positions are not the same – comparisons between individual positions is not possible.

3.8. Uncertainty

In this section, the applicability of modelling the system parameters as a multivariate Gaussian will be tested. The test will consist of comparing the mean flatness deviation and the uncertainty of the system parameters propagated to the measured deviation from the plane using a Monte-Carlo simulation. From M Monte-Carlo trials, the mean deviation and standard deviation of the results are found. Each pseudo-point is treated as an individual measurement that defines a perpendicular distance from a best-fit plane. The reduced χ^2 test value will be calculated for the entire plane. Given the number of samples used in the Monte-Carlo trials ($M = 1000$), it will be assumed that the distributions asymptotically approach normality [57].

The mean deviation and reduced χ^2 test values will all be investigated for the effect that the weighting matrix has on the parameter estimates and parameter uncertainty, as well as their general accuracy. The mean deviations from the best-fit plane, found by taking the mean of each point over its own set of points obtained from the Monte-Carlo trials, is given in Fig. 15. If the system parameters are modelled well as a multivariate Gaussian, the mean of the flatness deviation values should approach the flatness deviation as measured by the tactile CMS: $\pm 2\mu$m.

The mean flatness deviation values are generally inconsistent across different positions in the measurement volume and across different methods – despite both methods giving similar results in Fig. 14. Only in one position does the weighted serial method mean values approach the flatness deviation values as measured by the tactile CMS – which are significantly different to those obtained using just the mean parameter values as given in Fig. 14. These results show that the applicability of the multivariate Gaussian approach to the system parameters is highly dependant on the position of the flatness artefact in the measurement volume, i.e., the unique set of camera-projector coordinates, (u_c, v_c, u_p, v_p) that the measurement object covers. This result indicates that the specificity of the pinhole camera model with Brown-Conrady distortion is poor when considering the poorest flatness deviation value measured by the fringe projection system used in this paper: approximately $\pm$ 30μm. The standard deviation of the range of flatness deviation values per point is given in Fig. 16.

The standard deviation of the deviations from the best-fit plane is dependant on the plane position, with no weighted methods sharing a similar uncertainty across the flatness artefact. In Fig. 17, the mean and standard deviation values shown in Figs. 15 and 16 are used in a reduced χ^2 test to determine whether the system parameters with corresponding uncertainty matrix can account for the difference in flatness deviation values as measured using the tactile CMS.

The reduced χ^2 test scores are shown in Fig. 17. The ideal result of a reduced χ^2 test score is equal to one. The weighted serial method offers the best uncertainty evaluation, given the reduced χ^2 test scores closest to one, or under. The weighting matrix has improved the uncertainty estimation for both the serial and parallel methods. However, the uncertainty does not satisfactorily cover all positions for any one method. Generally, the weighting matrix improves the accuracy of the system parameters, particularly for the serial method. The efficacy of the weighted methods can be shown in the improvement of the unweighted parallel method over the serial method, but there is little difference in the accuracy of the system parameters between the two weighted methods. It is expected that the parallel method will outperform the serial method due to the fewer degrees of freedom – but the weighting matrix effectively negates this effect.

Notably, the mean of the deviation from the best-fit plane obtained using the Monte-Carlo trials does not equate to the deviation from the best-fit plane obtained using the mean system parameters. The mean parameter deviation is given in Fig. 14 and the Monte-Carlo mean is given in Fig. 15. The perturbation of system parameters will not give a corresponding perturbation of mean zero in the deviation from the plane.

The uncertainty of the system parameters provided by all methods is unable to account for all deviations of the flatness plate. There are many possible causes: the curvature of the non-linear regression being too high, parameter instability, poor specificity, or a poor estimation of the input covariance matrix. The curvature of the model was analysed and found to be appropriately linear within the solution locus and, therefore it is unlikely that the non-linearity of the model has prevented the evaluation of a reasonable uncertainty. The stability of the parameters were tested and it was found that the parameters were consistently stable throughout the characterisation measurements. The model specificity was tested and it was found to fail the specificity test – the implication is either that the input covariance matrix is incorrect, the model was mis-specified or both. In Fig. 17, the χ^2 values highly varied when measuring the plane across different points in the measurement volume. The dependency of the χ^2 values along with the failure of the specificity test strongly indicates that the pinhole and distortion models are insufficient to model both the camera and projector beyond levels of $\sim$ 30μm flatness (for a 300mm $\times$ 120mm flatness artefact).

4. Conclusion

In this paper, the common characterisation method to evaluate an uncertainty on the parameters estimated during the characterisation of fringe projection systems has been expanded. First, a method to evaluate uncertainty in the feature localisation method, as well construct and propagate a covariance matrix to the parameter estimates was outlined in Section 2. Two characterisation methods were outlined, the serial method and the parallel method, that regressed on camera and projector parameters together or separately. Then, a series of tests on the specificity, curvature and equilibrium of the characterisation regression problem were undertaken to validate assumptions made in the characterisation. It was found that the distortion model likely lacked the specificity to enable a reasonable estimate of parameter uncertainties. Lastly, the measurement of a flatness artefact was undertaken using all the estimated parameters from the characterisation. It was found that for the serial method, the covariance matrix improved the flatness measurement, and there was marginal improvement in the parallel method. Additionally, the parameter uncertainty matrix was unable to account for flatness measurement across the measurement volume, where it overestimated errors in certain positions, and underestimated in others. Consequently, it was concluded that the specificity of the parameters is insufficient to accurately model the flatness of this specific fringe projection system's measurements beyond levels of $\sim$ 30μm flatness (for a 300mm $\times$ 120mm flatness artefact). This work suggests that future work in evaluating uncertainty in system parameters should be dedicated to a non-parametric representation of distortion.

Author statement

The authors would like to thank each reviewer for their time and comments made on this manuscript.

Declaration of Competing Interest

The authors declare that they have no known competing financial interests or personal relationships that could have appeared to influence the work reported in this paper

Data availability

Data will be made available on request.

Acknowledgments

We would like to thank the Engineering and Physical Sciences Research Council (Grants EP/L01534X/1 and EP/M008983/1) and the Manufacturing Technology Centre (Coventry, UK).

References

[1] Hocken R J, Pereira PH. Multisensor coordinate metrology coordinate measuring machines and systems. 2nd ed. (CRC Press); 2011.
[2] Leach RK. Advances in optical form and coordinate metrology. 1st ed. IOPscience; 2020. doi:10.1088/978-0-7503-2524-0.
[3] Chen R, Xu J, Zhang S 2020 Digital fringe projection profilometry in: leach r k advances in optical form and coordinate metrology 1st ed. (IOPscience) Chap. 13
[4] Catalucci S, Thompson A, Piano S, Branson DT, Leach RK. Optical metrology for digital manufacturing: a review. Int J Adv Manuf Technol 2022;120:4271–90. doi:10.1007/s00170-022-09084-5.
[5] Kulkarni R, Banoth E, Pal P. Automated surface feature detection using fringe projection: an autoregressive modeling-based approach. Opt Lasers Eng 2019;121:506–11. doi:10.1016/j.optlaseng.2019.05.014.
[6] Ordoñes Nogales S, Servin M, Padilla M, Choque I, Flores Nuñez JL, Muñoz A. Shape defect measurement by fringe projection profilometry and phase-shifting algorithms. Opt Eng 2020;59(1). doi:10.1117/1.OE.59.1.014107.
[7] Xia R, Zhao J, Zhang T, Su R, Chen Y, Fu S. Detection method of manufacturing defects on aircraft surface based on fringe projection. Optik (Stuttg) 2020;208:164332. doi:10.1016/j.ijleo.2020.164332.
[8] Grasso M, Remani A, Dickins A, Colosimo BM, Leach RK. In-situ measurement and monitoring methods for metal powder bed fusion: an updated review. Meas Sci Technol 2021;32:112001. doi:10.1088/1361-6501/ac0b6b.
[9] Zhang B. In situ fringe projection profilometry for laser power bed fusion process 2017 diss. of The University of North Carolina; 2017.
[10] Southon N, Stavroulakis P, Goodridge R, Leach RK. In-process measurement and monitoring of a polymer laser sintering powder bed with fringe projection. Mater Des 2018;157:227–34. doi:10.1016/j.matdes.2018.07.053.
[11] Dickins A, Widjanarko T, Sims-Waterhouse D, Thompson A, Lawes S, Senin N, Leach RK. Multi-view fringe projection system for surface topography measurement during metal powder bed fusion. J Opt Soc Am A 2020;37 B93. doi:10.1364/JOSAA.396186.
[12] Velychko O, Gordiyenko T. Metrological traceability at different measurement levels. cucco L Standard, Methods and Solutions of Metrology 2019 Chap 1. doi:10.5772/intechopen.84853.
[13] ISO, IEC, OIML, BIPM. Guide to the Expression of Uncertainty in Measurement, ISO, Geneva 2008.
[14] Vagovský J, Buranský I, Görög A. Evaluation of measuring capability of the optical 3D scanner. Proced Eng 2015;100:198–1206. doi:10.1016/j.proeng.2015.01.484.
[15] Fei L, Dantan JY, Baudouin C, Du S. Calibration and uncertainty estimation of non-contact coordinate measurement systems based on Kriging models. Precis Eng 2019;57:16–29. doi:10.1016/j.precisioneng.2019.02.004.
[16] Zhang Z. A flexible new technique for camera calibration. IEEE Trans Pattern Anal Mach Intell 2000;22:1330–4. doi:10.1109/34.888718.
[17] Ranganathan A. The Levenberg-Marquardt algorithm. Tutor LM Algorithm 2004;11:101–10.
[18] Gavin HP. The levenberg-marquardt algorithm for nonlinear least squares curve-fitting problems. Dep Civ Environ Eng 2019:19.
[19] Transtrum, M. K., & Sethna, J. P. (2012). Improvements to the Levenberg-Marquardt algorithm for nonlinear least-squares minimization. *arXiv preprint arXiv:1201.5885*.
[20] Vo M, Wang Z, Pan B, Pan T. Hyper-accurate flexible calibration technique for fringe-projection-based three-dimensional imaging. Opt Express 2012;20:16926. doi:10.1364/OE.20.016926.
[21] Huang PS. Novel method for structured light system calibration. Opt Eng 2006;45:083601. doi:10.1117/1.2336196.
[22] Gupta M, Agrawal A, Veeraraghavan A, Narasimhan SG. A practical approach to 3D scanning in the presence of interreflections, subsurface scattering and defocus. Int J Comput Vis 2013;102:33–55. doi:10.1007/s11263-012-0554-3.
[23] Fischer M, Petz M, Tutsch R. Statistical characterization of evaluation strategies for fringe projection systems by means of a model-based noise prediction. J Sens Sens Syst 2017;6:145–53. doi:10.5194/jsss-6-145-2017.
[24] Yue H, Dantanarayana HG, Wu Y, Huntley JM. Reduction of systematic errors in structured light metrology at discontinuities in surface reflectivity. Opt Lasers Eng 2019;112:68–76. doi:10.1016/j.optlaseng.2018.08.002.
[25] Chen H, Yin Y, Cai Z, Xu W, Liu X, Meng X, Peng X. Suppression of the nonlinear phase error in phase shifting profilometry: considering non-smooth reflectivity and fractional period. Opt Express 2018;26:13489. doi:10.1364/OE.26.013489.
[26] Palousek D, Omasta M, Koutny D, Bednar J, Koutecky T, Dokoupil F. Effect of matte coating on 3D optical measurement accuracy. Opt Mater 2015;40:1–9. doi:10.1016/j.optmat.2014.11.020.
[27] OpenCV 4.5.5 *Open Source Computer Vision Library*., https://github.com/opencv/opencv/tree/4.5.5
[28] Vo M, Wang Z, Hoang T, Nguyen D. Flexible calibration technique for fringe-projection-based three-dimensional imaging. Opt Lett 2010;35:3192. doi:10.1364/OL.35.003192.
[29] Yang L, Normand JM, Moreau G. Practical and precise projector-camera calibration. In: Proceedings of the ISMAR (Merida, Mexico: IEEE); 2016. p. 63–70. doi:10.1109/ISMAR.2016.22.
[30] Li Bo, Heng L, Koser K, Pollefeys M. A multiple-camera system calibration toolbox using a feature descriptor-based calibration pattern. In: Proceedings of the IROS (Tokyo: IEEE); 2013. p. 1301–7. doi:10.1109/IROS.2013.6696517.
[31] Barone S, Neri P, Paoli A, Razionale AV. 3D acquisition and stereo-camera calibration by active devices: a unique structured light encoding framework. Opt Lasers Eng 2020;127:105989. doi:10.1016/j.optlaseng.2019.105989.
[32] Forster F. Camera calibration: active versus passive targets. Opt Eng 2011;50:113601. doi:10.1117/1.3643726.
[33] Wang Y, Chen X, Tao J, Wang K, Ma M. Accurate feature detection for out-of-focus camera calibration. Appl Opt 2016;55:7964. doi:10.1364/AO.55.007964.
[34] Mateos GG. A camera calibration technique using targets of circular features. In: Proceedings of the 5th SIARP (IEEE); 2000.
[35] Matsuoka R, Maruyama S. Eccentricity on an image caused by projection of a circle and a sphere. ISPRS Ann Photogramm Remote Sens Spat Inf Sci 2016:19–26 III–5. doi:10.5194/isprsannals-III-5-19-2016.
[36] Yang X, Fang S. Eccentricity error compensation for geometric camera calibration based on circular features. Meas Sci Technol 2014;25:025007. doi:10.1088/0957-0233/25/2/025007.
[37] Gong Z, Liu Z, Zhang G. Flexible global calibration of multiple cameras with nonoverlapping fields of view using circular targets. Appl Opt 2017;56:3122. doi:10.1364/AO.56.003122.
[38] Lai J, Li J, He C, Liu F. A robust and effective phase-shift fringe projection profilometry method for the extreme intensity. Optik (Stuttg) 2019;179:810–18. doi:10.1016/j.ijleo.2018.11.014.
[39] Zhang B, Davies A, Evans C, Ziegert J. Validity of the instrument transfer function for fringe projection metrology. Appl Opt 2018;57:2795. doi:10.1364/AO.57.002795.
[40] Ouellet JN, Hebert P. A simple operator for very precise estimation of ellipses. In: Proceedings of the 4th Conference CRV, Montreal, Canada; 2007. p. 21–8. IEEE. doi:10.1109/CRV.2007.8.
[41] Huang B, López S, Wu Z, Nascimento JM, Alpatov BA, Portell de Mora J, Schwenk K, Huber F. Connected component labelling algorithm for very complex and high-resolution images on an FPGA platform. Proc. SPIE 2015;9646:964603. doi:10.1117/12.2194101.
[42] Chou CC. A closed-form general solution for the distance of point-to-ellipse in two dimensions. J Interdiscip Math 2019;22:337–51. doi:10.1080/09720502.2019.1624064.
[43] Fitzgibbon AW, Pilu M, Fisher RB. Direct least squares fitting of ellipses. In: Proceedings of the 13th ICRV, Vienna, Austria (IEEE), 1; 1996. p. 253–7. vol. doi:10.1109/ICPR.1996.546029.
[44] Amiri-Simkooei A, Jazaeri S. Weighted total least squares formulated by standard least squares theory. J Geod Sci 2012;2:113–24. doi:10.2478/v10156-011-0036-5.
[45] Fang X, Wang J, Li B, Zeng W, Yao Y. On total least squares for quadratic form estimation. Stud Geophys Geod 2015;59:366–79. doi:10.1007/s11200-014-0267-x.
[46] Guo H, Chen M, Zheng P. Least-squares fitting of carrier phase distribution by using a rational function in fringe projection profilometry. Opt Lett 2006;31:3588. doi:10.1364/OL.31.003588.
[47] Xing S, Guo H. Iterative calibration method for measurement system having lens distortions in fringe projection profilometry. Opt Express 2020;28:1177. doi:10.1364/OE.382595.
[48] Wang J, Zhang Z, Leach RK, Lu W, Xu J. Predistorting projected fringes for high-accuracy 3-D phase mapping in fringe projection profilometry. IEEE Trans Instrum Meas 2021;70:1–9. doi:10.1109/TIM.2021.3067961.
[49] Li K, Bu J, Zhang D. Lens distortion elimination for improving measurement accuracy of fringe projection profilometry. Opt Lasers Eng 2016;85:53–64. doi:10.1016/j.optlaseng.2016.04.009.
[50] Yang S, Liu M, Song J, Yin S, Ren Y, Zhu J, Chen S. Projector distortion residual compensation in fringe projection system. Opt Lasers Eng 2019;114:104–10. doi:10.1016/j.optlaseng.2018.10.015.
[51] Hecht E. Optics. 4th Edition. San Francisco: Addison Wesley; 2002.
[52] White H. Consequences and detection of misspecified nonlinear regression models. J Amer Statist Assoc 1981;76:419–33.
[53] Clarke GPY. Marginal curvatures and their usefulness in the analysis of nonlinear regression models. J Amer Statist. Assoc 1987;82:844–50.
[54] Bates DM, Watts DG. Relative curvature measures of nonlinearity. J R Stat Soc Ser B Methodol 1980;42:1–16. doi:10.1111/j.2517-6161.1980.tb01094.x.
[55] Molimard J, Navarro L. Uncertainty on fringe projection technique: a Monte-Carlo-based approach. Opt Lasers Eng 2013;51:840–7. doi:10.1016/j.optlaseng.2013.01.023.
[56] Ding C, He X. K-means clustering via principal component analysis. In: Proceedings of the 21st ICML, Banff, Canada (ACM), 29; 2004.
[57] Ghasemi A, Zahediasl S. Normality tests for statistical analysis: a guide for non-statisticians. Int J Endocrinol Metab 2012;10:486–9. doi:10.5812/ijem.3505.